Simulation studies of the coplanar electrode and other plasma display panel cell designs

G. Veronis and U. S. Inan[a)]
Space, Telecommunications, and Radioscience Laboratory, Stanford University, Stanford, California 94305

(Received 13 August 2001; accepted for publication 21 March 2002)

A two-dimensional self-consistent simulation model is used to study the effect of the geometric parameters on the operating voltages and ultraviolet (UV) efficiency of a coplanar-electrode plasma display panel cell. It is found that in the standard coplanar-electrode geometry there is a tradeoff between high UV efficiency and low operating voltages as the electrode gap, or the parameters of the upper dielectric are varied, while variation of the sustain electrode width has no significant effect on either the operating voltages or UV efficiency. It is also found that wider discharge area results in higher efficiency. In addition, the effect of the insertion of floating electrodes in the upper dielectric is investigated. When floating electrodes are used, UV light is emitted in a more confined area, thus limiting cross talk with adjacent cells, while efficiency decreases by ~8%. Finally, a self-erase discharge sustaining waveform is studied. Use of this waveform results in ~17% increase in the UV efficiency. © *2002 American Institute of Physics.* [DOI: 10.1063/1.1478143]

I. INTRODUCTION

Plasma display panels (PDPs) are one of the leading candidates in the competition for large-size, high-brightness flat panel displays, suitable for high definition television (HDTV) monitors.[1,2] Their advantages are high resolution, wide viewing angle, low weight, and simple manufacturing process for fabrication. Recent progress of PDP technology development and manufacturing has been remarkable.[3,4] One of the most critical issues in ongoing PDP research is the improvement of the luminous efficiency, which is still low compared to conventional cathode ray tube displays (CRTs). Another important problem is the relatively high operating voltages.

PDP cells are small (cell height is ~150 μm) and provide limited access for diagnostic measurements. As a result, experimental studies of plasma discharges in PDPs are extremely difficult. PDP parameters measured experimentally fall short of providing a quantitative understanding of the discharge dynamics. As a result, computer-based modeling is currently essential for understanding PDP physics and optimizing its operation. Computer simulations are effective in identifying the basic properties of the discharge and the dominant mechanisms of light emission. In addition, simulation models are usually successful in predicting the effects on the performance of the device of variations in design parameters, such as cell geometry, applied voltage waveforms, and gas mixture. Although simulation results are usually in qualitative rather than quantitative agreement with experimental measurements, they are used very effectively to provide directions for future PDP design.

Typical plasma displays consist of two glass plates, each with parallel electrodes deposited on their surfaces. The electrodes are covered with a dielectric film. The plates are sealed together with their electrodes at right angles, and the gap between the plates is filled with an inert gas mixture. A protective MgO layer is deposited above the dielectric film. The role of this layer is to decrease the breakdown voltage due to the high secondary electron emission coefficient of MgO. The UV photons emitted by the discharge hit the phosphors deposited on the walls of the PDP cell and are converted into visible photons. Each cell contains phosphor that emits one primary color, red, green, or blue.

The most common type of color plasma display is the coplanar-electrode PDP. In this PDP type, each cell is formed by the intersection of a pair of transparent sustain electrodes on the front plate, and an address electrode on the back plate. In operation, a periodic voltage with a frequency of 50–350 kHz is continuously applied between each pair of sustain electrodes. The amplitude of the sustain voltage is below the breakdown voltage. A cell is turned on by applying a write voltage pulse between the address electrode and one of the sustain electrodes. The discharge which is initiated results in the deposition of surface charge on the dielectric layers covering these two electrodes. The superposition of the electric field due to the deposited surface charge and of the electric field due to the applied sustaining voltage results in the ignition of sustain discharges between the pair of sustain electrodes.

In this article, we use a two-dimensional (2D) self-consistent model to simulate the microdischarges in a coplanar-electrode PDP cell. We investigate the effect of the variation of the cell design parameters on the operating voltages and UV efficiency of the device. In addition, we use the model to study two alternative designs which have been proposed to improve the performance of the standard coplanar-electrode PDP.[5,6] First, we investigate the effect of the insertion of floating conducting materials in the dielectric layer covering the sustain electrodes. Second, we investigate the effect of applying a nonstandard voltage waveform including assistant voltage pulses between the sustain electrodes. In Sec. II, we describe the model used. In Sec. III, we present

[a)]Electronic mail: inan@nova.stanford.edu

the results of our model for the standard coplanar-electrode PDP and the two alternative designs. Our conclusions are summarized in Sec. IV.

II. MODEL DESCRIPTION

A. Fluid model

The dynamics of the PDP plasma are described using a 2D fluid model. For each species s, the spatial and temporal variations of the density are calculated by solving the continuity equation

$$\frac{\partial n_s}{\partial t} + \nabla \cdot \mathbf{\Gamma_s} = S_s, \tag{1}$$

where n_s is the number density, $\mathbf{\Gamma_s}$ is the particle flux, and S_s is the source term determined by the particle production and loss processes for species s. We consider electrons, atomic (Ne^+, Xe^+) and molecular ($Ne_2^+, Xe_2^+, NeXe^+$) ions, and excited species [$Ne_m^*, Xe^*(^3P_1), Xe^*(^3P_2), Xe^{**}$, $Xe_2^*(O_u^+), Xe_2^*(^3\Sigma_u^+)$, $Xe_2^*(^1\Sigma_u^+)$] for a Ne–Xe mixture. Since the gas pressure in typical PDP conditions is high, we use the drift-diffusion equation as an approximation to the momentum equation

$$\mathbf{\Gamma}_s = \mathrm{sgn}(q_s) n_s \mu_s \mathbf{E} - D_s \nabla n_s, \tag{2}$$

where q_s is the particle charge, μ_s is the particle mobility, $\mathbf{E}$ is the electric field, and D_s is the diffusion coefficient.

The electric field within the cell is self-consistently calculated by solving Poisson's equation

$$\nabla \cdot (\varepsilon \mathbf{E}) = \sum_s q_s n_s, \tag{3}$$

where ε is the dielectric permittivity.

Electron impact reaction rates and transport coefficients are assumed to be functions of the electron mean energy. The electron mean energy is determined by solving the electron energy equation

$$\frac{\partial n_\varepsilon}{\partial t} + \nabla \cdot \mathbf{\Gamma}_\varepsilon = S_\varepsilon, \tag{4}$$

where $n_\varepsilon = n_e \overline{\varepsilon}$ is the electron energy density, n_e is the electron density, and $\overline{\varepsilon}$ is the electron mean energy. It can be shown[7] that if the momentum equation is approximated by the drift-diffusion equation, and the heat flux vector $\mathbf{q_e}$ is taken as

$$\mathbf{q_e} = -\lambda \nabla T_e, \tag{5}$$

where λ is the thermal conductivity and T_e is the electron temperature, then we have

$$\mathbf{\Gamma}_\varepsilon = -\tfrac{5}{3} n_\varepsilon \mu_e \mathbf{E} - \tfrac{5}{3} D_e \nabla n_\varepsilon, \tag{6}$$

and

$$S_\varepsilon = -e \mathbf{\Gamma_e} \cdot \mathbf{E} - n_e \sum_i \nu_i \varepsilon_i, \tag{7}$$

where $\mathbf{\Gamma}_\varepsilon$ is the electron energy flux, and S_ε is the electron energy source term. In Eq. (7) the first term on the right-hand side represents electron heating by the electric field, while the second term accounts for the electron energy losses due to inelastic collisions. The summation in the second term is over all of the electron impact reactions with occurrence frequency ν_i, with ε_i being the corresponding electron loss energy.

In several PDP models[8–11] the so-called local field approximation is used to calculate electron impact reaction rates and transport coefficients instead of using Eq. (4). In these models, rates and transport coefficients are presumed to be functions of the local reduced electric field E/N. The local field approximation does not take into account the electron energy redistribution due to thermal conduction and convection described by the electron energy flux $\mathbf{\Gamma}_\varepsilon$ in Eq. (4). In addition, local field approximation models often use an effective electric field, calculated with additional approximations, instead of the exact local electric field.[9] Additional approximations are not required when the electron energy equation is used. A more detailed comparison of the two methods presented at the end of Sec. III A shows that the local field approximation introduces substantial error in the results when used instead of the electron energy equation. We therefore feel that it is more appropriate to use the electron energy equation instead of the local field approximation for calculation of electron impact reaction rates and transport coefficients.

As in Ref. 12, constant values at a given pressure are used for the transport coefficients of ions and neutral species, so that their energy equations do not have to be solved.

B. Numerical method and input data

We use a finite difference method to solve the system of partial differential Eqs. (1), (3), and (4). The Scharfetter–Gummel scheme[13] is used for the discretization of Eq. (2), as in Ref. 8. The continuity equations and the electron energy equation are solved implicitly in time to avoid the Courant–Friedrich–Levy constraint on the timestep. During the discharge pulse, the presence of high charged species densities severely limits the dielectric relaxation time. As a result, if an explicit method of integration were used for the continuity and field equations, the maximum allowable timestep would be constrained to be less than a ps. However, several pulses have to be simulated before the device reaches periodic steady state resulting in a required total simulation time of several μs. We therefore chose to integrate the continuity and field equations using the semi-implicit method introduced in Ref. 14. This method requires the solution of a modified Poisson equation with allowable timesteps orders of magnitude larger than the dielectric relaxation time. In addition, when the electron energy equation is used, it becomes limiting for the timestep if an explicit treatment of the source term S_ε is used in Eq. (4). Small timesteps are required to avoid numerical oscillations in the solution of Eq. (4). We therefore chose to treat this term implicitly, using the method introduced in Ref. 15. Sparse linear systems resulting from the discretization of Eqs. (1), (3), and (4) are solved using an implementation of the biconjugate gradient sparse matrix solution method with incomplete LU factorization for preconditioning.[16] In summary, the continuity equations and

the electron energy equation are solved implicitly, and semi-implicit methods are used for the integration of the coupled continuity and field equations, and for the source term in the electron energy equation.

For the numerical treatment of floating electrodes we used the capacity matrix method.[17] In this method Poisson's equation is solved twice per timestep. First, the total charge, which is assumed to be zero in the case of floating electrodes inserted in the dielectric layer, is distributed uniformly in the surface of the floating electrodes. Poisson's equation is then solved and the distribution of electric potential (not necessarily constant) on the surface of floating electrodes is obtained. It can be shown that the surface charge density on the floating electrodes can be calculated using the nonconstant potential distribution obtained by Poisson's equation, and the capacity matrix precalculated at the beginning of the simulation, by imposing the condition of charge conservation and of constant potential on each floating electrode. After calculating the surface charge density, Poisson's equation is solved again and a constant potential is obtained on the surface of each floating electrode.

The electron impact ionization and excitation frequencies as well as the electron mobility are calculated using the Boltzmann code ELENDIF,[18] which calculates the electron energy distribution function under uniform electric fields. Once the electron mean energy is calculated using Eq. (4), the solution of the Boltzmann equation obtained by ELENDIF is used to determine ionization and excitation frequencies as well as electron mobility. Electron-atom collision cross sections for Ne and Xe are taken from the SIGLO Series.[19] Ion mobilities were obtained from Ref. 20 and Blanc's law[21] was used to calculate ion mobilities in gas mixtures. Rate coefficients for Penning ionization, dimer ions formation, charge, exchange, recombination, and neutral kinetics reactions as well as excited species lifetimes are taken from Ref. 8. As in Meunier *et al.*,[8] a Holstein escape factor is used to describe the lengthening of the apparent lifetime of the resonant state $Xe^*(^3P_1)$ due to radiation trapping, and the resonance radiation is assumed to be optically thin. Electron and ion diffusion coefficients are determined using the Einstein relation

$$\frac{D}{\mu} = \frac{k_B T}{e}, \tag{8}$$

where k_B is the Boltzmann constant, T is the particle temperature, and e is the elementary charge. The ion temperature is assumed to be equal to the gas temperature.

C. Cell geometry and boundary conditions

The geometry of the PDP cell used in the simulations is shown in Fig. 1. In our studies we focus on the coplanar-electrode PDP design. The cell consists of two sustain electrodes, *X* and *Y*, separated from the gas by a dielectric layer. A MgO layer is deposited on the dielectric film. The bottom of the cell consists of the address electrode *A* separated from the gas by a dielectric layer with a phosphor layer on top. Floating electrodes inserted in the upper dielectric are included in some of the simulations.

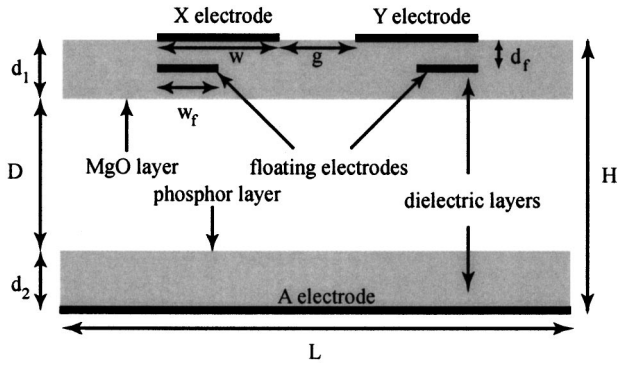

FIG. 1. Schematic of the coplanar-electrode plasma display panel (PDP) cell used in the simulations. The floating electrodes inserted in the upper dielectric layer are included in the results of Sec. III B.

The secondary electron emission coefficients for Ne and Xe ions on MgO are taken to be $\gamma_{Ne}=0.5$ and $\gamma_{Xe}=0.01$, respectively,[22] while for the molecular ions we assume $\gamma_{Ne_2}=0.5\gamma_{Ne}$ and $\gamma_{NeXe}=\gamma_{Xe_2}=0.5\gamma_{Xe}$. Few data exist for secondary electron emission coefficients on phosphors, which are smaller than the corresponding coefficients on the MgO layer.[23] The secondary electron emission coefficient for Ne ions on the phosphor layer is taken to be $\gamma_{Ne}=0.1$.[23] For all other ions we assume the ratio of the secondary electron emission coefficients on the MgO and phosphor layers to be the same as the corresponding ratio for Ne ions.

Boundary particle fluxes to the walls include a drift term and a thermal flux term.[8] A secondary electron flux term is included in the electron boundary flux. Reflective boundary conditions are used at the lateral ends of the cell for the continuity equations. The perpendicular electric field is set to zero at the lateral ends of the cell and at the portions of the upper boundary which are not covered by metal.[22] Surface charge density distributions are calculated on the gap–dielectric interface and on the floating electrodes, if included, as described above.

III. RESULTS

A. Standard coplanar-electrode geometry

In this section, we study the effect of the variation of the cell geometry parameters on the performance of the device. The floating electrodes shown in Fig. 1 are not included in these studies. In all cases, the gas mixture filling the region between the dielectrics is a 4% Xe–Ne mixture at a pressure of 500 Torr. The basic cell geometry is as shown in Fig. 1, but without the floating electrodes. The height and width of the cell are $H=210$ μm and $L=1260$ μm, respectively. The length of the lower dielectric layer is $d_2=30$ μm. We investigate the effect of the variation of the electrode gap length g, the sustain electrode width w, the length of the upper dielectric layer d_1 and the dielectric constant ε_r on the operating voltages and the efficiency of the PDP cell. Our reference case is characterized by the parameter values $g=100$ μm, $w=300$ μm, $d_1=30$ μm, and $\varepsilon_r=10$.

The voltages applied to the three electrodes during the simulation are shown in Fig. 2(a). Initially, a data pulse V_D and a base-write pulse $-V_{SW}$ are applied simultaneously to

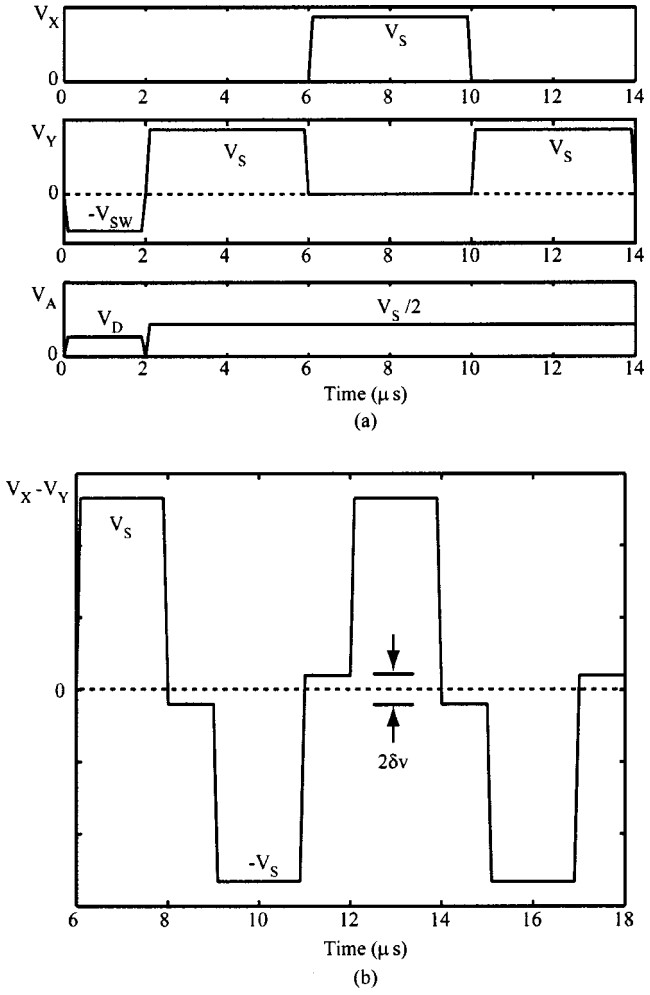

FIG. 2. (a) Driving scheme used in the simulations showing the voltage applied to the *X*, *Y*, and *A* electrodes. Initially, a 2 μs address pulse is applied, followed by a sequence of alternating polarity sustain pulses. The sustaining frequency is 125 kHz. The address electrode is biased to a voltage of $V_S/2$ during the sustaining phase. (b) The self-erase discharge waveform used in the simulations of Sec. III C. The sustaining frequency is 167 kHz. The 2 μs sustain pulses are followed by a 1 μs assistant pulse. The address electrode is floating during the sustaining phase.

the *A* and *Y* electrode, respectively. These are followed by a sequence of alternating sustaining voltage pulses V_S between the two sustain electrodes *X* and *Y*. During the sustain phase the address electrode *A* is biased to a voltage of $V_S/2$ to prevent undesired discharges between the address electrode and the sustain electrodes. The frequency of the sustaining waveform is 125 kHz and the rise and fall times of all pulses are 100 ns. The duration of the address pulses is 2 μs.

1. Voltage margin

We first study the effect of geometric parameters on the operating voltages of the device. PDP cells can operate only if the applied sustaining voltage is held within certain limits. The initial address pulse triggers a discharge between the *A* and *Y* electrodes. This discharge is quenched by surface charges accumulated on the dielectrics. Subsequent sustain discharges occur only in the addressed cells, since the sustain voltage V_S is below the breakdown voltage, as discussed above. The minimum sustaining voltage $V_{S\,\min}$ is defined as

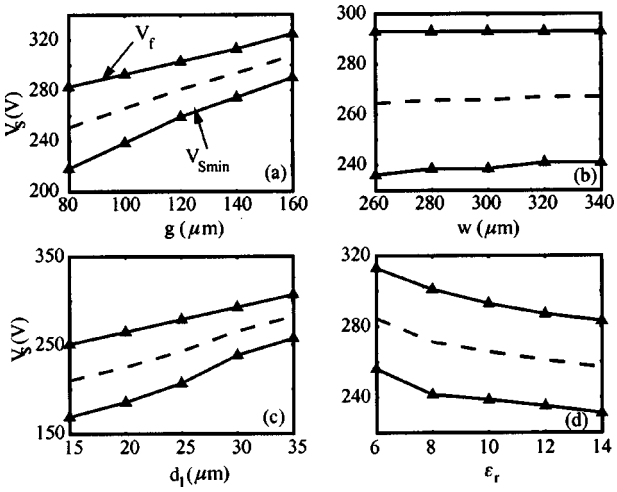

FIG. 3. (a) Firing voltage V_f and the minimum sustaining voltage $V_{S\,\min}$ as a function of the sustain electrode gap *g*. The dashed line shows the mid-margin sustaining voltage V_{Sm} used for the calculation of UV efficiency; (b) V_f, $V_{S\,\min}$, and V_{Sm} as a function of the sustain electrode width *w*; (c) V_f, $V_{S\,\min}$, and V_{Sm} as a function of the upper dielectric layer length d_1; (d) V_f, $V_{S\,\min}$, and V_{Sm} as a function of the dielectric constant ε_r.

the minimum value of V_S which leads to a steady sequence of sustaining discharges in an addressed cell.[24] The firing voltage V_f is defined as the breakdown voltage in an unaddressed cell. $V_{S\,\min}$ and V_f define the voltage margin of the cell. In real PDPs these voltages exhibit some statistical variation, since cells have slightly different dimensions.[24] The voltage margin of the cell should therefore be as large as possible to ensure reliable operation of the display.

In our studies, we investigate the effect of the design parameters *g*, *w*, d_1, ε_r (Fig. 1) on $V_{S\,\min}$ and V_f. For the calculation of V_f a sustain pulse V_S is applied to one of the sustain electrodes and *A* is biased to $V_S/2$, as described above. We use the 2D model to iteratively calculate (to within an accuracy of a volt) the minimum voltage V_f which leads to breakdown. In all cases the breakdown occurs between the two sustain electrodes.

For the calculation of $V_{S\,\min}$ we first apply the address pulses V_D and V_{SW} described above. In all cases, we use $V_{SW}=150$ V, and for the reference case $V_D=80$ V. In all other cases, V_D is chosen so that the breakdown parameter[25] $\mu=(\alpha_{\mathrm{Ne}}\gamma_{\mathrm{Ne}}+\alpha_{\mathrm{Xe}}\gamma_{\mathrm{Xe}})\quad[e^{(\alpha_{\mathrm{Ne}}+\alpha_{\mathrm{Xe}})D}-1]/(\alpha_{\mathrm{Ne}}+\alpha_{\mathrm{Xe}})$ is constant, where α_{Ne} and α_{Xe} are the partial first Townsend ionization coefficients for Ne and Xe, respectively, and *D* is the discharge gap (Fig. 1). A sequence of sustaining pulses V_S is then applied between the sustain electrodes [Fig. 2(a)]. We use the 2D model (in an iterative fashion) to calculate (to within an accuracy of a volt) the minimum voltage $V_{S\,\min}$ which leads to a steady sequence of sustain discharges.

The results are shown in Fig. 3. V_f is an increasing function of *g*, as expected. Larger *g* results in longer discharge paths between the two sustain electrodes, requiring larger voltages for breakdown. The voltage margin, defined as $V_f-V_{S\,\min}$, decreases with *g*, due to the fact that if *g* is increased while *D* is kept constant, the breakdown voltage between the two sustain electrodes increases while the breakdown voltage between the sustain and address electrodes

remains constant. The address-sustain discharge path then becomes increasingly favorable over the sustain–sustain path, thus limiting the window of stable operation of the device. Variation of the sustain electrode width w has no significant effect on V_f or $V_{S\,\min}$. The electric field distribution in the region between the two sustain electrodes is not significantly perturbed as w is varied, so that V_f and $V_{S\,\min}$ remain almost constant with w. We see that V_f is an increasing function of d_1. As d_1 is increased, the voltage drop in the gap decreases if the applied voltage is kept constant. Thus, higher voltages are required to cause breakdown. The voltage margin is a decreasing function of d_1. We note that the cell height H is kept constant in our calculations, so that as d_1 decreases, the gap D increases. Thus, the sustain–sustain discharge path becomes increasingly favorable over the address–sustain path and the window of stable sustain operation becomes wider. Finally, V_f is a decreasing function of the dielectric constant ε_r. As ε_r is increased, the voltage drop in the gap increases for constant applied voltage. Thus, lower voltages are required to cause breakdown. The variation of ε_r has no significant effect on the voltage margin of the cell, since in both the sustain–sustain and address–sustain paths the voltage drop is increased as ε_r is increased.

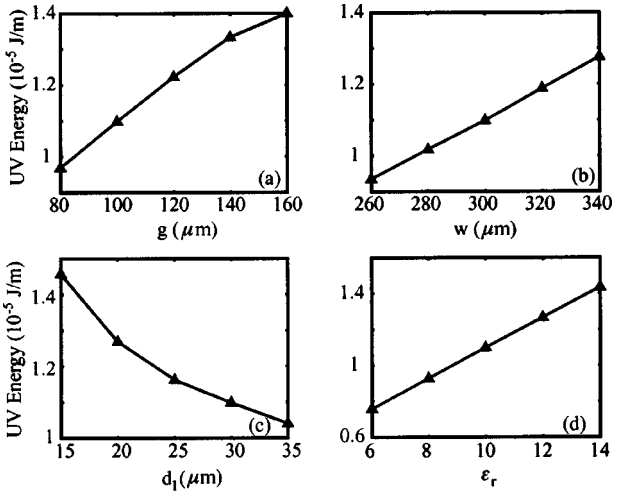

FIG. 4. (a) Total UV energy emitted per sustain pulse as a function of the sustain electrode gap g; (b) total UV energy emitted per sustain pulse as a function of the sustain electrode width w; (c) total UV energy emitted per sustain pulse as a function of the upper dielectric layer length d_1; (d) total UV energy emitted per sustain pulse as a function of the dielectric constant ε_r.

2. Total UV energy and UV efficiency

We next study the effect of geometric parameters of the PDP cell on UV emission. UV photons which excite the phosphors and produce visible light are emitted by certain excited states of Xe [$Xe^*(^3P_1)$ (resonant state) at 147 nm, $Xe_2^*(O_u^+)$ at 150 nm, $Xe_2^*(^3\Sigma_u^+)$, and $Xe_2^*(^1\Sigma_u^+)$ at 173 nm (excimer states)].[8] We define the UV efficiency of the cell as the ratio of total UV emitted energy integrated over all wavelengths considered (147 nm, 150 nm, and 173 nm) to the total dissipated energy during a sustaining period

$$\eta_{\mathrm{UV}}=\frac{\int_T dt\int_V dx dy \sum_{i=1}^{N_{\mathrm{UV}}} n_i \nu_i \varepsilon_{\mathrm{UV}i}}{\int_T dt\int_V dx dy (\mathbf{J}_e+\sum_{i=1}^{N_{\mathrm{ion}}}\mathbf{J}_{\mathrm{ion}i})\cdot\mathbf{E}}, \tag{9}$$

where n_i is the number density of UV emitting excited state of Xe i, ν_i, and $\varepsilon_{\mathrm{UV}i}$ are the corresponding emission frequency and emitted photon energy, respectively, and $\mathbf{J}_e$ and $\mathbf{J}_{\mathrm{ion}i}$ are the electronic and ionic current (of ion i), respectively. We note that, as mentioned above, the kinetic scheme used in our model is the same as in Ref. 8.

A similar study has been previously done by Rauf and Kushner.[26] In their work, the applied sustaining voltage used for the calculation of efficiency was kept constant as the geometric parameters were varied. In addition, the efficiency calculation was based on the first sustaining pulse following an initial address pulse. In our work, the voltage waveform shown in Fig. 2(a) is applied in all cases to the cell electrodes. The sustaining voltage is chosen to be the midmargin voltage, shown in Fig. 3 with a dashed line, defined as $V_{Sm}=(V_{S\,\min}+V_f)/2$ rather than a constant reference voltage. The midmargin voltage is usually chosen as the point of operation of the PDP to ensure reliability. If a constant reference voltage were used for the calculation of efficiency, the value used might be outside the operating window in some cases, as can be seen in Fig. 3. In addition, we calculate the UV efficiency of the PDP cell in the periodic steady state. We found that during the first few sustaining pulses the device is in a transient state. The efficiency during this transition time may be quite different (by as much as a factor of 3) from the steady state efficiency.

Figure 4 shows the total UV energy emitted per sustain pulse as a function of the geometric parameters of the cell. The UV energy is an increasing function of the gap length g. As the gap length g increases, the discharge path length also increases. As a result, the total energy dissipated by electrons, the energy spent in Xe excitation and consequently the UV emission energy increase. The UV energy is also an increasing function of the sustain electrode width w. As mentioned above, the breakdown initially occurs in the region between the two sustain electrodes where the electric field is higher. As the dielectric surface above the electrodes is covered with charge, the discharge path moves towards the outer ends of the electrodes. This process continues until all the dielectric surface above the electrodes is covered with charge. The total duration of the current pulse is therefore proportional to the electrode width, and the total dissipated energy by electrons, the energy spent in Xe excitation and the UV emission energy increase as the electrode width is increased. Finally, we observe that the UV energy per sustain pulse increases as d_1 is decreased or ε_r is increased. Both decreasing d_1 or increasing ε_r result in increasing the capacitance of the upper dielectric layer.[26] As the capacitance of the dielectric layer is increased more energy has to be dissipated during the discharge before it is quenched by surfaces charges. We note that as d_1 is decreased or ε_r is increased the operating voltages decrease (see Fig. 3). However, the effect of increased capacitance dominates, since the rate of change of the capacitance with respect to d_1 or ε_r is much higher than the rate of change of the midmargin operating voltage with respect to the same parameters.

Figure 5 shows the UV efficiency, as defined in Eq. (9),

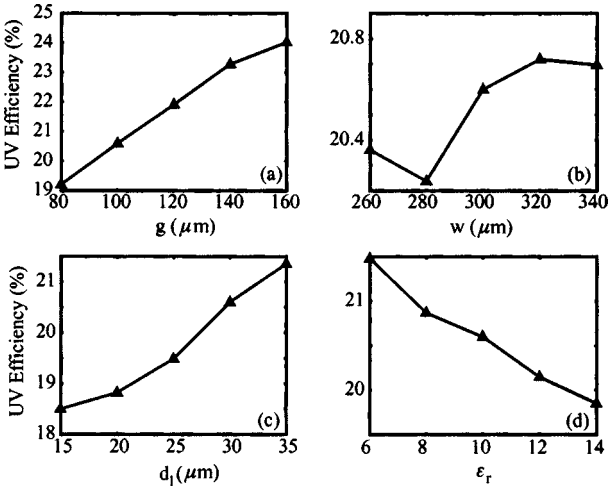

FIG. 5. (a) UV efficiency as a function of the sustain electrode gap g; (b) UV efficiency as a function of the sustain electrode width w; (c) UV efficiency as a function of the upper dielectric layer length d_1; (d) UV efficiency as a function of the dielectric constant ε_r.

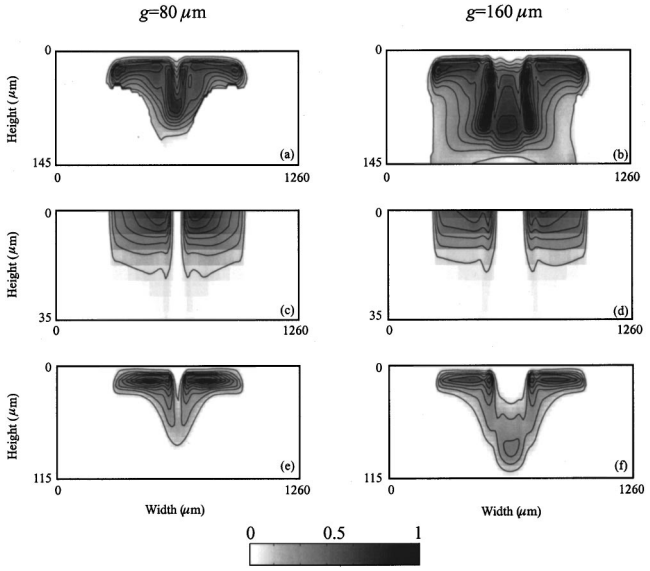

FIG. 6. (a), (b) Local excitation efficiency for the $g=80\ \mu$m and the $g=160\ \mu$m cases. The increment between the contours is 0.1. The maximum in the gray scale corresponds to 1. (c), (d) Normalized dissipated energy density for the $g=80\ \mu$m and the $g=160\ \mu$m cases. The increment between the contours is 2.10×10^{7} m^{-2}. The maximum in the gray scale corresponds to 2.10×10^{8} m^{-2}. (e), (f) Normalized density of energy spent in Xe excitation for the $g=80\ \mu$m and the $g=160\ \mu$m cases. The increment between the contours is 2.83×10^{6} m^{-2}. The maximum in the gray scale corresponds to 2.83×10^{7} m^{-2}. Note the different vertical scale in each plot . In all cases height is measured from the MgO layer surface.

as a function of the geometric parameters of the cell. We observe that by increasing the gap from 80 to 160 μm the UV efficiency increases by ~25%. Variation of the electrode width w results in insignificant change in the efficiency. Increasing the upper dielectric layer length from 15 to 35 μm results in an ~15% increase in efficiency. Finally, decreasing the dielectric constant ε_r from 14 to 6 results in an ~8% increase in efficiency.

In order to interpret these results, we focus our attention on the excitation efficiency defined as

$$\eta_{\mathrm{exc}}=\frac{\int_T dt\int_V dxdy\sum_{i=1}^{N_{\mathrm{exc}}} n_e \nu_i^* \varepsilon_{\mathrm{exc}i}}{\int_T dt\int_V dxdy(\mathbf{J}_e+\sum_{i=1}^{N_{\mathrm{ion}}}\mathbf{J}_{\mathrm{ion}i})\cdot\mathbf{E}}, \tag{10}$$

where ν_i^* is the excitation frequency of excited state of Xe i which leads through a series of reactions to UV photon production, and $\varepsilon_{\mathrm{exc}i}$ is the corresponding electron loss energy. The UV efficiency η_{UV} is always lower than the excitation efficiency η_{exc} because in the series of reactions that lead to UV photon production part of the energy of the Xe excited states is lost through cascading to lower states, and because some excited atoms are lost through diffusion to the walls. In all cases considered, we found that η_{UV} and η_{exc} are directly related and the effect of the variation of any geometric parameter is the same on both. This is expected since in all cases the gas mixture composition and consequently the rate coefficients of reactions involving excited species are the same. Due to the long lifetimes of some of the excited states of Xe which lead to UV emission, some UV photons are emitted several μs after the corresponding electron impact excitation reaction. In addition, due to particle diffusion and to reabsorption of resonance radiation at 147 nm, the physical location of UV photon emission can be different from that of the corresponding electron impact excitation reaction. As a result, UV emission does not coincide with the corresponding energy dissipation neither temporally nor spatially. On the other hand, if the local equilibrium approximation is assumed, the energy gain from the electric field is locally (in space and in time) balanced by the loss due to collisions. In other words, in the case of excitation efficiency a spatially and temporally local quantity defined as

$$\eta(x,y,t)=\frac{\sum_{i=1}^{N_{\mathrm{exc}}} n_e \nu_i^* \varepsilon_{\mathrm{exc}i}}{(\mathbf{J}_e+\sum_{i=1}^{N_{\mathrm{ion}}}\mathbf{J}_{\mathrm{ion}i})\cdot\mathbf{E}},$$

is meaningful, while a similar quantity cannot be defined in the case of UV efficiency for the reasons given above. Nevertheless, careful examination of the local excitation efficiency $\eta(x,y,t)$ can give useful insight into the factors that govern UV efficiency.

The excitation efficiency can also be written as

$$\eta_{\mathrm{exc}}=\int_V dxdy\left[\int_T dt\frac{p_{\mathrm{exc}}}{\varepsilon_{\mathrm{tot}}}\right]=\int_V dxdy\left[\frac{\int_T dtp_{\mathrm{exc}}}{\int_T dtp}\frac{\int_T dtp}{\varepsilon_{\mathrm{tot}}}\right], \tag{11}$$

where $p_{\mathrm{exc}}=\sum_{i=1}^{N_{\mathrm{exc}}} n_e \nu_i^* \varepsilon_{\mathrm{exc}i}$, $p=(\mathbf{J}_e+\sum_{i=1}^{N_{\mathrm{ion}}}\mathbf{J}_{\mathrm{ion}i})\cdot\mathbf{E}$, and $\varepsilon_{\mathrm{tot}}=\int_T dt\int_V dxdyp$. In Fig. 6 we show the quantities $f_1(x,y)=\int_T dtp_{\mathrm{exc}}/\int_T dtp$, $f_2(x,y)=\int_T dtp/\varepsilon_{\mathrm{tot}}$ and $f(x,y)=f_1(x,y)f_2(x,y)$ for the $g=80\ \mu$m and the $g=160\ \mu$m cases (the rest of the parameters are those of the reference case). It can be seen from Eq. (11) that f_1 is the spatially local excitation efficiency, f_2 is normalized dissipated energy, and $f=f_1f_2$ is a quantity which, if spatially integrated, gives the excitation efficiency, i.e., $\eta_{\mathrm{exc}}=\int_V dxdyf(x,y)$. We observe that f is wider in the $g=160\ \mu$m case, while the maximum value of f is higher in the $g=80\ \mu$m case. The discharge path between the two sustain electrodes is wider for wider g, as explained above. The overall excitation effi-

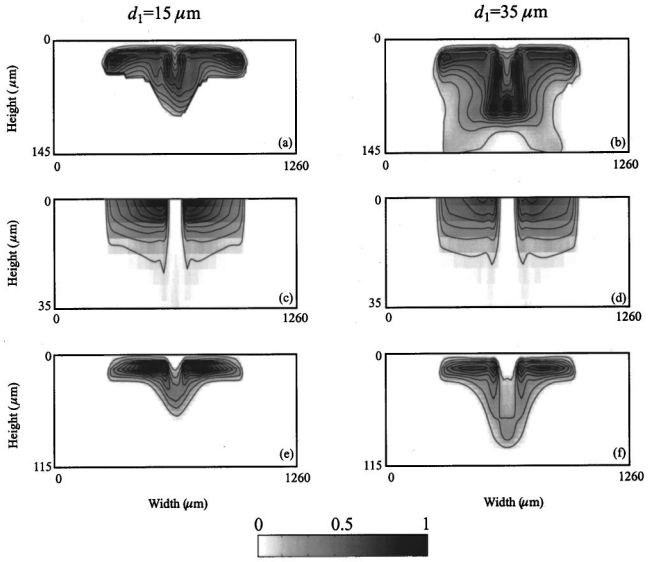

FIG. 7. (a), (b) Local excitation efficiency for the $d_1=15\ \mu$m and the $d_1=35\ \mu$m cases. The increment between the contours and maximum in gray scale are the same as in Figs. 6(a) and 6(b). (c),(d) Normalized dissipated energy density for the $d_1=15\ \mu$m and the $d_1=35\ \mu$m cases. The increment between the contours and maximum in gray scale are the same as in Figs. 6(c) and 6(d). (e),(f) Normalized density of energy spent in Xe excitation for the $d_1=15\ \mu$m and the $d_1=35\ \mu$m cases. The increment between the contours and maximum in gray scale are the same as in Figs. 6(e) and 6(f). Note the different vertical scale in each plot. In all cases height is measured from the MgO layer surface.

ciency is higher in the $g=160\ \mu$m case. In both cases we observe that the dissipated energy, i.e., f_2, is high in the region directly below the dielectric layer covering the sustain electrodes, where the sheath is formed during the discharge. There is also some energy dissipation in the area between the two electrodes. We also observe that the local excitation efficiency is high in the region between the two electrodes in both cases. It is also high a few microns away from the dielectric layer. A similar picture is observed in Fig. 7 when comparing the $d_1=15\ \mu$m and $d_1=35\ \mu$m cases. We observe that f is wider in the $d_1=35\ \mu$m case, while the maximum value of f is higher in the $d_1=15\ \mu$m case with the overall excitation efficiency being higher in the $d_1=35\ \mu$m case. In this case, as d_1 is decreased, D increases (because H is kept constant) so that the sustain–sustain path becomes increasingly favorable over the sustain–address path, as explained above, and the sustain discharge becomes more confined in the region directly below the upper dielectric layer. The dissipated energy is high in the region directly below the dielectric layer covering the sustain electrodes, and the local excitation efficiency is higher in the region between the two electrodes. A similar picture is observed in all cases we examined.

Our conclusion from the study of the excitation efficiency is that the wider the discharge area the higher the overall efficiency. In all cases, the discharge area can be divided into two regions: The first is the sheath region where most of the energy dissipation takes place. The efficiency is not very high in this region, since most of the energy is dissipated by the ions. The second is the region between the two electrodes where the initial discharge path is formed. Energy in this region is mostly dissipated by electrons and the efficiency is high. The local excitation efficiency can also be written as

$$\eta(x,y,t)=\frac{\Sigma_{i=1}^{N_{\rm exc}} n_e \nu_i^* \varepsilon_{{\rm exc}i}}{\mathbf{J}_e\cdot\mathbf{E}}\,\frac{\mathbf{J}_e\cdot\mathbf{E}}{(\mathbf{J}_e+\Sigma_{i=1}^{N_{\rm ion}}\mathbf{J}_{{\rm ion}i})\cdot\mathbf{E}}$$

$$=\eta_1(x,y,t)\,\eta_2(x,y,t),$$

where η_1 is a measure of how efficiently the electrons excite Xe atoms, while η_2 is a measure of how efficiently the electrons are heated by the electric field. It is interesting to note that both η_1 and η_2 are higher in the region between the two electrodes. The electric field is lower during the discharge in the region between the two electrodes compared to the high electric field of the sheath region directly below the dielectric layer. The quantity η_1 is higher for lower electric fields[27] (this is true for $E\simeq E_k$, where E_k is the breakdown electric field), while η_2 is also higher in the region between the electrodes, since the sheath region is dominated by the ionic current.

The overall efficiency increases as the highly efficient discharge region between the two electrodes becomes wider. It is for this reason that the UV efficiency of the discharge increases as g or d_1 is increased or as ε_r is decreased. From a practical point of view, we note that in all three cases the increase in efficiency is accompanied by an increase in the operating voltages. We can conclude that in the standard coplanar-electrode geometry there is a tradeoff between high UV efficiency and low operating voltages. If the electrode width w is varied, there is no significant change in the efficiency, as mentioned above, since the spatial extent of the discharge region between the two electrodes does not change. We finally note that the dependence of efficiency on the geometric parameters of the cell is directly related to the spatial extent of the discharge, so that uncertainties in model data such as cross sections and rate coefficients do not have a significant effect on this result.

Figures 8(a) and 8(b) show the normalized density of energy spent in Xe excitation calculated using the electron energy equation and the local field approximation, respectively. Results are presented for the reference case. In the case of the local field approximation we use the effective-electric field expression introduced in Ref. 9. In agreement

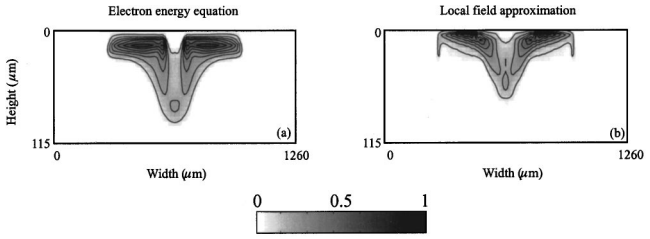

FIG. 8. (a) Normalized density of energy spent in Xe excitation calculated using the electron energy equation. (b) Normalized density of energy spent in Xe excitation calculated using the local field approximation. Results are presented for the reference case. The increment between the contours and maximum in gray scale are the same as in Figs. 6(e) and 6(f). Height is measured from the MgO layer surface.

with Ref. 12, we observe that use of the local field approximation substantially modifies the discharge characteristics. The more detailed treatment of electron impact reaction rates and transport coefficients with the electron energy equation results in a wider discharge region. We found that the local field approximation underestimates the electron ionization and excitation coefficients in the bulk plasma region because it does not take into account energy transport from the cathode region to the colder bulk plasma region through thermal conduction and drift of warm electrons from the cathode region.[12] As a result, a more confined discharge region is predicted, which, in agreement with our previous discussions, results in substantially lower discharge efficiency. We found that when the local field approximation is used instead of the electron energy equation the excitation efficiency is ~32% lower for the reference case. Similarly large errors in the calculation of discharge efficiency when the local field approximation is used instead of the electron energy equation are reported in Ref. 28.

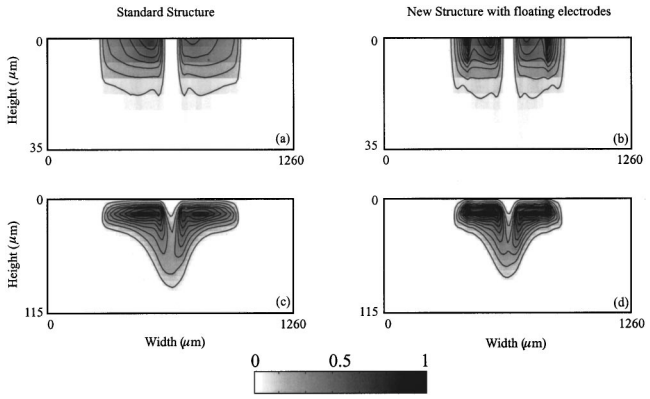

FIG. 9. (a), (b) Dissipated energy density for the standard and new structure, respectively. The increment between the contours is 2.94×10^{3} J m^{-3}. The maximum in the gray scale corresponds to 2.94×10^{4} J m^{-3}. (c), (d) UV emission energy density for the standard and new structure, respectively. The increment between the contours is 174 J m^{-3}. The maximum in the gray scale corresponds to 1.74×10^{3} J m^{-3}. Note the different vertical scale in each plot. In all cases height is measured from the MgO layer surface.

B. Effect of floating electrodes

In this section, we investigate the effect of the insertion of floating electrodes in the upper dielectric layer. The geometry of the PDP cell with floating electrodes is as shown in Fig. 1. The use of floating electrodes has been proposed as a way to improve the performance of the PDP cell.[5]

In our studies, we choose the width of the floating electrodes to be $w_f=150$ μm, and the distance from the sustain electrodes to be $d_f=20$ μm (Fig. 1). All other parameters were chosen to be the same as in the reference case. In addition, the same driving scheme was used [Fig. 2(a)]. Since the floating electrodes are inserted in the region below the outer ends of the sustaining electrodes, no significant change in the breakdown voltage of the cell is expected. We found that for $w_f \leqslant 200$ μm the breakdown voltage is the same as in the reference case to within an accuracy of a volt. We therefore applied the same sustaining voltage to compare the floating-electrode PDP cell with the reference coplanar-electrode PDP cell, which for brevity will heretofore be referred to as the new and standard structures, respectively.

In Figs. 9(a) and 9(b), we show the dissipated energy density during one sustaining period [Fig. 2(a)] for the standard and new structure cases, respectively. In both cases, high dissipated energy density is observed in the regions directly below the dielectric layer covering the sustaining electrodes. We also observe that the high dissipated energy density region is more localized in the new structure case. In Figs. 9(c) and 9(d), we show the total UV emission energy density integrated over all wavelengths considered (147, 150, and 173 nm) during one sustaining period for the standard and new structure cases, respectively. We observe that UV emission is confined to the regions below the dielectric surface covering the sustaining electrodes. However, in both cases the region of high UV emission is wider (note the different vertical scales for Figs. 9(a) and 9(b) versus Figs. 9(c) and 9(d)) when compared to the region of high dissipated energy density [shown in Figs. 9(a) and 9(b)], extending towards the lower dielectric layer. This result is due to diffusion of some of the excited states of Xe which have long lifetimes. In addition, UV emission is more localized in the new structure case, since the region where power is spent by electrons in Xe excitation is more localized, as explained above [Figs. 9(a) and 9(b)]. The discharge current and UV emission confinement of the discharge by the new structure is expected to reduce cross talk between adjacent cells in agreement with the experimental findings reported in Ref. 5. The total UV energy emitted per sustain pulse in the new structure case was found to be approximately equal to the UV energy emitted in a coplanar-electrode PDP cell with electrode width $w=260$ μm (Fig. 4). However, the emitted UV energy is more confined in the new structure case. The confinement of the discharge in the new structure case results in a ~8% decrease in UV efficiency. Overall, the advantage of the new structure over the standard structure is that the same total amount of UV light can be emitted in a more confined area, thus limiting cross talk with adjacent cells, at the expense of some reduction in efficiency.

Figures 10(a) and 10(b) show the dissipated total power, dissipated electron power, and power spent on Xe excitation in the PDP cell per unit length for the standard and new structure cases, respectively. Results are shown as a function of time, during the discharge caused by the fourth sustain pulse applied to the X electrode starting at $t=14$ μs. We observe that the shape of the discharge power pulses are quite different, in agreement with the experimental results for the discharge current waveform.[5] For the case of the new cell structure, the voltage waveform has a double-pulse shape. Figures 10(c) and 10(d) show snapshots of the surface charge density deposited on the upper dielectric layer for the standard and new structure cases, respectively. Figure 10(d) also shows snapshots of the induced surface charge density on the floating electrodes. The times corresponding to the snapshots are also shown in Figs. 10(a) and 10(b) with dots for comparison. It should be noted that during the discharge caused by the fourth pulse, the X electrode acts as the anode, while the Y electrode acts as the cathode. In the standard

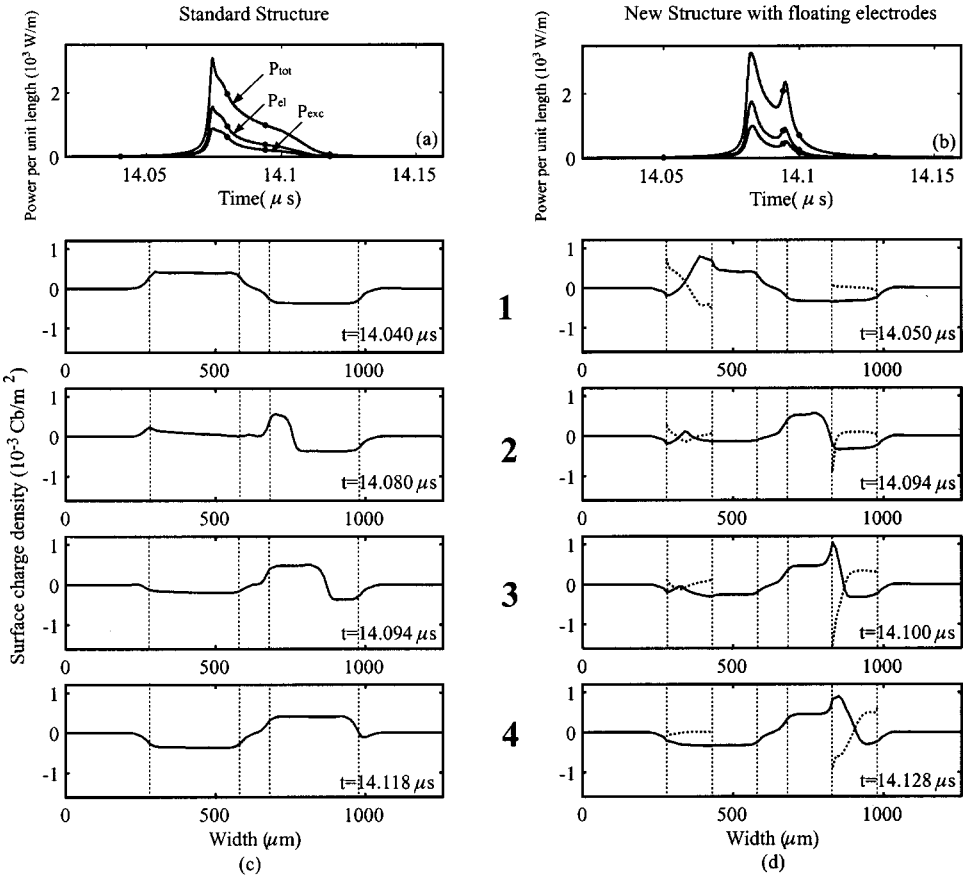

FIG. 10. (a), (b) Dissipated total power P_{tot}, dissipated electron power P_{el}, and power spent on Xe excitation P_{exc} per unit length for the standard and new structure, respectively; (c) snapshots of the surface charge density on the upper dielectric layer for the standard structure; (d) snapshots of the surface charge density on the upper dielectric layer and on the floating electrodes (with dashed lines) for the new structure. The positions of electrodes are shown with dashed lines.

case, we observe that initially the surface charge distribution is symmetric with respect to the center of the sustain electrode gap. As the dielectric layer below the cathode is covered with positive charge, the discharge path moves towards the outer ends of the electrodes. This process continues until all the dielectric layer below the cathode is covered with positive charge, as previously discussed. In the new structure case, a quite different behavior is observed. The floating electrode below the cathode initially has a small charge density. The initial phase of the discharge does not differ substantially from the standard case [Figs. 10(a) and 10(b) and snapshots 1, 2 of Figs. 10(c) and 10(d)]. However, in the new structure case as the discharge path moves towards the inner end of the floating electrode below the cathode, the surface charge on the floating electrode is redistributed. Negative charge is attracted on the inner end of the floating electrode by the positive surface charge deposited on the dielectric layer and the positive space charge in the sheath region [snapshot 2 of Fig. 10(d)]. As negative charge is accumulated in the inner end of the floating electrode, the electric field in the discharge path is enhanced, more positive charge has to be deposited on the dielectric layer before the discharge is quenched, and the discharge current consequently increases [Fig. 10(b)]. In addition, since the total charge of the floating electrode is zero, positive charge is accumulated on the outer end of the floating electrode. The electric field of the sustain electrodes is screened by the positive charge, so that the discharge continues only until the dielectric layer below approximately the inner half of the floating electrode is covered with positive charge. This phenomenology explains the spatial confinement of the discharge in the new structure case, which was apparent in Figs. 9(a) and 9(b).

C. Effect of self-erase discharge waveform

In this section, we investigate the effect of using an alternative sustaining waveform. Figure 2(b) shows the self-erase discharge waveform used for the simulations discussed in this section. The frequency of the waveform is 167 kHz and the rise and fall times of all pulses are 100 ns. The duration of the sustain pulse is 2 μs. Each sustain pulse is followed by an assistant pulse of opposite polarity and 1 μs duration. The use of the self-erase discharge waveform has been proposed as a way to improve the efficiency of the PDP cell.[6] In the self-erase discharge waveform there is an idle period, between the application of the sustain pulses. Under certain conditions, surface charges on the upper dielectric layer deposited by the previous sustain discharge and space charges may cause a self-erase discharge during the idle period. Part of the charge deposited by the previous sustain discharge is erased. An assistant pulse may be applied during the idle period to promote the self-erase discharge.[6]

We compared the waveform shown in Fig. 2(a) with the self-erase discharge waveform shown in Fig. 2(b) which will heretofore be referred to as the standard and new waveforms, respectively. When the new waveform is used, the address electrode is floating during the application of the sustaining waveform to prevent discharges between the address and sustain electrodes. The reference coplanar-electrode PDP cell was used (without the floating electrodes). The amplitude of

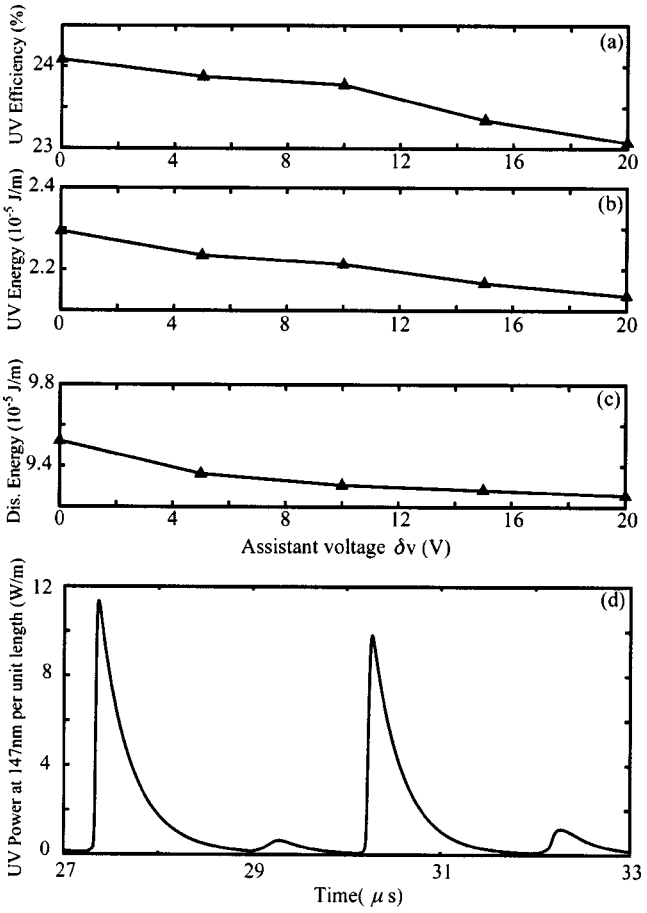

FIG. 11. (a) UV efficiency as a function of the amplitude of the assistant pulse δv. (b) Total UV energy emitted per period as a function of the amplitude of the assistant pulse δv. (c) Dissipated energy per period as a function of the amplitude of the assistant pulse δv. (d) UV emission power per unit length at 147 nm for $\delta v = 0$. The two UV pulses caused by two subsequent sustain discharges have different amplitude. The two smaller UV pulses are caused by self-erase discharges during the idle period [Fig. 2(b)].

the sustaining voltage pulse is the same in both cases. We also investigate the effect of the variation of the amplitude of the assistant pulse δv [Fig. 2(b)].

If no assistant pulse is used, the UV efficiency of the new waveform is ~17% higher than the UV efficiency of the standard waveform, in good agreement with the experimentally observed increase in the luminous efficiency.[6] When the new waveform is used, a self-erase discharge during the idle period erases part of the surface charge deposited by the previous sustain discharge, as mentioned above. As a result, the duration of the next sustain discharge, which is determined by the time required to cover the dielectric layer below the cathode with positive charge, is shorter. Every sustain discharge is characterized by an initial period where the electronic current dominates and a subsequent less efficient period where the ionic current in the sheath dominates. When the new waveform is used, the second less efficient period is shorter so that the overall efficiency is higher. Figures 11(a), 11(b), and 11(c) show the calculated UV efficiency, UV energy, and dissipated energy per period, respectively, as a function of the assistant voltage δv. When comparing Fig. 11(b) with Fig. 4, it should be taken into account that time integration is over one period (6 μs) in the first case, and over one sustain pulse (4 μs) in the second case [Figs. 2(a) and 2(b)]. The experimentally observed increase in luminance and luminous efficiency,[6] when the assistant pulse is applied, is not reproduced by the simulation. When the standard waveform is used, UV light emission is periodic with period equal to one half of the sustaining period, due to the fact that UV pulses produced by sustaining pulses of opposite polarity are identical. When the new waveform is used, two subsequent sustain discharge pulses and consequently the two corresponding light pulses are not identical, as shown in Fig. 11(d). The two smaller UV pulses are caused by self-erase discharges during the idle period. This result is also observed in the experiment.[6] We found that in a sequence of two sustain discharge pulses, one has shorter duration and is more efficient for the reasons described above. In the experiment,[6] it was observed that the luminance and luminous efficiency are maximized for $\delta v = 10$ V. This observation may be due to the fact that for the specific experimental conditions (cell geometry, driving scheme, gas mixture) this particular amplitude of the assistant pulse represents an optimal match between two subsequent sustain discharge pulses so that the overall efficiency is maximized.

IV. SUMMARY

We used a two-dimensional self-consistent model to investigate the effect of the variation of the cell design parameters on the operating voltages and UV efficiency of a coplanar-electrode PDP cell. As the sustain electrode gap g or the upper dielectric length d_1 is increased, or as the dielectric constant ε_r is decreased both the efficiency and the operating voltages increase. If the sustain electrode width w is varied, there is no significant change in either the efficiency or in the operating voltages. Analysis of the factors that determine the UV efficiency showed that the wider the discharge area the higher the efficiency. In addition, we used the model to investigate the effect of the insertion of floating electrodes in the upper dielectric layer. We found that, if this new structure is used, the same total amount of UV light can be emitted in a more confined area, thus limiting cross talk with adjacent cells, while efficiency decreases by ~8%. Finally, we investigated the effect of applying a self-erase discharge sustaining voltage waveform. Use of this new waveform results in ~17% increase of the UV efficiency, although the experimentally observed further increase of the efficiency when assistant pulses are used was not reproduced by the simulation.

ACKNOWLEDGMENTS

The authors greatly appreciate discussions with Professor Victor Pasko of Pennsylvania State University. This research was supported by the Office of Technology Licensing of Stanford University under Grant No. 127P316 and by the National Science Foundation under Grant No. ATM-9731170.

[1] A. Sobel, Sci. Am. **278**, 70 (1998).
[2] *Electronic Display Devices*, edited by S. Matsumoto (Wiley, New York, 1990), p. 131.
[3] Y. Kanazawa, T. Ueda, S. Kuroki, K. Kariya, and T. Hirose, SID'99 Dig. 1999, p. 154.
[4] Y. Hashimoto, Y. Seo, O. Toyoda, K. Betsui, T. Kosaka, and F. Namiki, SID'01 Dig. 2001, p. 1328.
[5] J. S. Kim, C. H. Jeon, E. C. Lee, Y. J. Ahn, S. D. Kang, S. Y. Ahn, Y. K. Shin, J. H. Ryu, and J. D. Schemerhorn, SID'00 Dig. 2000, p. 102.
[6] T. Hashimoto and A. Iwata, SID'99 Dig. 1999, p. 540.
[7] J. A. Bittencourt, *Fundamentals of Plasma Physics* (FAPESP, Sao Jose dos Campos, 1995), p. 204.
[8] J. Meunier, Ph. Belenguer, and J. P. Boeuf, J. Appl. Phys. **78**, 731 (1995).
[9] C. Punset, J. P. Boeuf, and L. C. Pitchford, J. Appl. Phys. **83**, 1884 (1998).
[10] R. Veerasingam, R. B. Campbell, and R. T. McGrath, IEEE Trans. Plasma Sci. **23**, 688 (1995).
[11] R. Veerasingam, R. B. Campbell, and R. T. McGrath, IEEE Trans. Plasma Sci. **24**, 1399 (1996).
[12] S. Rauf and M. J. Kushner, J. Appl. Phys. **85**, 3460 (1999).
[13] D. L. Scharfetter and H. K. Gummel, IEEE Trans. Electron Devices **ED-16**, 64 (1969).
[14] P. L. G. Ventzek, R. J. Hoekstra, and M. J. Kushner, J. Vac. Sci. Technol. B **12**, 461 (1994).
[15] G. J. M. Hagelaar and G. M. W. Kroesen, J. Comput. Phys. **159**, 1 (2000).
[16] SLAP sparse matrix library, http://www.netlib.org
[17] R. W. Hockney and J. W. Eastwood, *Computer Simulation Using Particles* (McGraw-Hill, New York, 1981), p. 215.
[18] W. L. Morgan and B. M. Penetrate, Comput. Phys. Commun. **58**, 127 (1990).
[19] http://www.siglo-kinema.com/database/xsect/siglo.sec
[20] H. W. Ellis, R. Y. Pai, E. W. McDaniel, E. A. Mason, and L. A. Viehland, At. Data Nucl. Data Tables **17**, 177 (1976); H. W. Ellis, E. W. McDaniel, D. L. Albritton, L. A. Viehland, S. L. Lin, and E. A. Mason, *ibid.* **22**, 179 (1978); H. W. Ellis, M. G. Thackston, E. W. McDaniel, and E. A. Mason, *ibid.* **31**, 113 (1984).
[21] A. Blanc, J. Phys. **7**, 825 (1908).
[22] C. Punset, S. Cany, and J. P. Boeuf, J. Appl. Phys. **86**, 124 (1999).
[23] V. Elsbergen, P. K. Bachmann, and T. Juestel, SID'00 Dig. 2000, p. 220.
[24] T. Shinoda, M. Wakitani, T. Nanto, N. Awaji, and S. Kanagu, IEEE Trans. Electron Devices **47**, 77 (2000).
[25] Y. P. Raizer, *Gas Discharge Physics* (Springer, Berlin, 1997), p. 131.
[26] S. Rauf and M. J. Kushner, J. Appl. Phys. **85**, 3470 (1999).
[27] G. Veronis, U. S. Inan, and V. P. Pasko, IEEE Trans. Plasma Sci. **28**, 1271 (2000).
[28] G. J. M. Hagelaar, M. H. Klein, R. J. M. M. Snijkers, and G. M. W. Kroesen, J. Appl. Phys. **89**, 2033 (2001).